

Measurements of the Temperature Structure-Function Parameters with a Small Unmanned Aerial System Compared with a Sodar

Timothy A. Bonin · David C. Goines · Aaron K. Scott ·
Charlotte E. Wainwright · Jeremy A. Gibbs ·
Phillip B. Chilson

Received: 4 August 2014 / Accepted: 4 February 2015 / Published online: 24 February 2015
© Springer Science+Business Media Dordrecht 2015

Abstract The structure function is often used to quantify the intensity of spatial inhomogeneities within turbulent flows. Here, the Small Multifunction Research and Teaching Sonde (SMARTSonde), an unmanned aerial system, is used to measure horizontal variations in temperature and to calculate the structure function of temperature at various heights for a range of separation distances. A method for correcting for the advection of turbulence in the calculation of the structure function is discussed. This advection correction improves the data quality, particularly when wind speeds are high. The temperature structure-function parameter C_T^2 can be calculated from the structure function of temperature. Two case studies from which the SMARTSonde was able to take measurements used to derive C_T^2 at several heights during multiple consecutive flights are discussed and compared with sodar measurements, from which C_T^2 is directly related to return power. Profiles of C_T^2 from both the sodar and SMARTSonde from an afternoon case exhibited generally good agreement. However, the profiles agreed poorly for a morning case. The discrepancies are partially attributed to different averaging times for the two instruments in a rapidly evolving environment, and the measurement errors associated with the SMARTSonde sampling within the stable boundary layer.

Keywords Sodar · Temperature structure-function parameter · Turbulence · Unmanned aerial system

T. A. Bonin (✉) · C. E. Wainwright · P. B. Chilson
Advanced Radar Research Center and School of Meteorology,
University of Oklahoma, Norman, OK, USA
e-mail: tim.bonin@ou.edu

D. C. Goines · A. K. Scott · J. A. Gibbs
School of Meteorology, University of Oklahoma, Norman, OK, USA

1 Introduction

The vertical structure of the atmosphere typically exhibits significant changes in temperature, pressure, humidity, and wind with height. While the horizontal distribution of these atmospheric parameters is generally more homogeneous compared with their vertical distribution, the presence of turbulent eddies increases horizontal variability. If turbulence is locally isotropic and homogenous, these spatial thermodynamic variations lead to Bragg scattering of electromagnetic and acoustic waves (Neff and Coulter 1986), which can be used to characterize the structure of atmospheric turbulence through remote sensing instruments (Wyngaard and LeMone 1980). The effects of turbulence on wave propagation can be described by the refractive-index structure function for electromagnetic waves (Tatarskii 1971; Gossard et al. 1982) and temperature structure function for acoustic waves (Weill et al. 1980).

Kolmogorov (1941) discussed the concept of a velocity structure function as a means of quantifying turbulence. Since then, the concept of structure functions has become generalized to apply to practically any quantity in turbulent flows. Structure functions are defined as the mean square of a differential quantity at a particular separation distance. Specifically, the temperature structure function, D_T , is defined as

$$D_T(r) = \langle [\Delta T(r)]^2 \rangle, \quad (1)$$

in which ΔT is the difference in temperature across a particular separation distance r and the angle brackets denote ensemble averaging (Obukhov 1949). If the turbulence is isotropic, homogeneous, volume filling, and within the inertial subrange, the structure function can be normalized using an inverse 2/3 law in separation distance (Kolmogorov 1941), yielding the temperature structure-function parameter, C_T^2 , as

$$C_T^2 = \frac{D_T(r)}{r^{2/3}}, \quad (2)$$

in which r is the separation distance.

Remote sensors have been used to quantify temperature and refractive-index structure-function parameters. Radars, usually with a wavelength ≥ 0.1 m, are capable of measuring the refractive index structure-function parameter, C_n^2 , by using a relationship with reflectivity in clear air (i.e. no insects, clouds, precipitation, or other point scatterers). Initially, vertically pointing very high frequency (VHF) radars were used to examine scattering layers at heights well above the planetary boundary layer (PBL), such as within the stratosphere and mesosphere (e.g., Röttger 1980). However, as the technology has improved and the pulse length has become shorter, vertically pointing ultra high frequency (UHF) wind-profiling radars have been able to examine the upper portion of the PBL (Fairall 1991). Recently, with the advent of dual-polarization technology, S-band radars with a wavelength of 0.1 m have been able to identify when returned signals are from clear air, and have been used to derive C_n^2 in the PBL, including range-height cross-sections that depict variations in the top of the boundary layer over terrain (Melnikov et al. 2013). Laser, large-aperture and microwave scintillometers have been used to quantify path-integrated C_n^2 over a distance ranging from ~ 100 m for laser scintillometers to ~ 10 km for large-aperture scintillometers. Scintillometers typically operate at heights at or below 50 m above ground level (a.g.l.) and provide a measurement of C_n^2 at the average measurement height, and are therefore not useful for profiling. There have been numerous field projects utilizing scintillometers over inhomogeneous terrain such as patchy agricultural fields (e.g., Meijninger et al. 2002; Beyrich et al. 2012), urban areas (e.g., Kanda et al. 2002; Lagouarde et al. 2006) and sub-urban areas (e.g., Ward et al. 2014), grasslands (e.g., Asanuma and Iemoto 2007), and open water in coastal regions (e.g., Mahon et al. 2009).

While radars and scintillometers are the principle remote sensors used to measure C_n^2 , the primary remote sensor used to measure C_T^2 profiles in the boundary layer is the sodar. Sodar-returned power, P_R , is proportional to the structure-function parameter for temperature through

$$P_R \propto \frac{C_T^2}{T^2} \frac{\exp(-2\alpha z)}{z^2}, \quad (3)$$

where T is temperature in K, α is the acoustic attenuation in dB m^{-1} , z is height in m, and C_T^2 is in units of $\text{K}^2 \text{ m}^{-2/3}$ (Coulter and Wesely 1980). By introducing a proportionality constant k , Eq. 3 can be rewritten as

$$P_R = k \frac{C_T^2}{T^2} \frac{\exp(-2\alpha z)}{z^2}. \quad (4)$$

Once the sodar is properly calibrated (e.g., Neff 1975) and k is quantified, C_T^2 can be derived. In the literature, sodars have been extensively used to quantify turbulence through Eq. 4. For example, recently sodars have been used to examine turbulence in relation to monsoons (Shravan Kumar et al. 2011), study the fine-scale structure of sea breezes (Puygrenier et al. 2005), evaluate turbulence in the Arctic boundary layer (Bonner et al. 2009; Petenko et al. 2014a), and determine the statistics of C_T^2 within the convective boundary layer (Petenko et al. 2014b). However, C_T^2 determined from sodars is often reported as uncalibrated, as calibration requires a complex procedure (Danilov et al. 1994).

Several different instrument platforms are also able to make in situ measurements of C_T^2 . Temperature measurements from instrumented towers with pairs of spatially-separated fast-response thermistors can be used to calculate C_T^2 at a given separation distance, r (Haugen and Kaimal 1978). However, it is also possible to use a single temperature sensor with a time delay, accounting for the advection of frozen turbulence past the sensor (Kohsiek 1982). Manned aircraft have also been used to quantify C_T^2 (e.g., Thomson et al. 1978), by measuring fluctuations in temperature along a trajectory. Earlier, Konrad et al. (1970) suggested that small remotely-controlled aircraft would be able to make similar measurements. The advance of technology has recently enabled such observations, as an unmanned aerial system (UAS) has been used to measure C_T^2 along a flight path (van den Kroonenberg et al. 2012). Quantifying turbulence throughout the boundary layer is becoming a special application for these platforms in atmospheric studies (e.g., Holland et al. 2001; Shuqing et al. 2004; van den Kroonenberg et al. 2008; Mayer et al. 2010; Elston et al. 2011b), since they are able to take in situ measurements at known spatial locations throughout the entire boundary layer at a much lower cost than when using manned aircraft.

Here, we investigate a new method for measuring the temperature structure-function parameter in the boundary layer with a UAS and compare these UAS structure-function measurements with those derived from sodar backscatter. Previous studies where aircraft or UAS measurements are used to calculate C_T^2 utilize flight paths along a straight line (i.e., van den Kroonenberg et al. 2012; Maronga et al. 2013), which are ideal for comparing similar measurements from scintillometers along a line-of-sight path. However, within the present study, a circular flight plan is used that allows for C_T^2 to be determined over a smaller area, allowing for a more direct comparison with a sodar that has a small sampling volume. Additionally, a correction for the advection of frozen turbulence is introduced for the calculation of C_T^2 , which has not been considered in previous studies where C_T^2 is determined from UAS observations.

The structure of the paper is as follows: Sect. 2 provides a description of the instrumentation used and the approval to fly the UAS by regulatory agencies. In Sect. 3, the method by which

C_T^2 is calculated from UAS measurements is discussed, including a description of the UAS flight plan. Section 4 discusses the environmental conditions during the considered flights, as well as comparisons between the sodar-derived C_T^2 and C_T^2 values determined from the UAS. Section 5 summarizes the results.

2 Instrumentation and Experimental Set-Up

Data for this experiment were collected at the University of Oklahoma's Kessler Atmospheric and Ecological Field Station (KAEFS) on six days between March–July 2013. The site is a 1.46 km² research and education facility located in rural central Oklahoma (see Fig. 1) that is owned by the University of Oklahoma, and consists of a mixed landscape of tall grasses, woodlands, pastures, and several ponds on gently rolling terrain that varies by ≈ 25 m in elevation. Several temporary and permanent meteorological instruments are deployed at the KAEFS site, including those relevant to boundary-layer measurements.

2.1 Instrumentation

Data from a Metek PCS.2000-24 Doppler sodar, Doppler lidar, Oklahoma Mesonet station, and the Small Multifunction Autonomous Research and Teaching Sonde (SMARTSonde) collected at the KAEFS site are used. The location of each instrument is provided in Fig. 1. The minimum sampling range of the sodar is 25 m and the maximum range is specified as 500 m, although 250 m is typical under most conditions at the KAEFS site. The range resolution is 10 m and a 5-min averaging period is used. The sodar is uncalibrated, so the constant k in Eq. 4 is not known before the experiment.

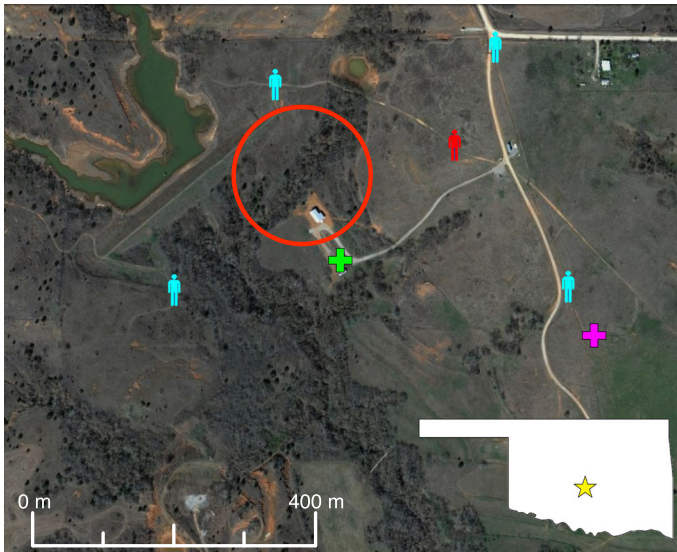


Fig. 1 Satellite image of the KAEFS site depicting the location of the pilot in command (*red person*), observers (*cyan people*), sodar and lidar (*green cross*), Washington Mesonet site (*purple cross*), and location of where the SMARTSonde typically circled (*red circle*). The *star* in the map in the lower right shows where the KAEFS site is located in the state of Oklahoma, USA

A Streamline Halo pulsed heterodyne Doppler lidar was deployed at the KAEFS site from before the experiment through mid-May 2013. This lidar was configured to nominally point vertically to take vertical velocity measurements; however, during the course of the experiment presented here it also collected velocity azimuth display (VAD) wind profiles every 30 min. The Oklahoma Mesonet station, the Washington site, is maintained by the Oklahoma Climatological Survey and is one of 110 such stations across the state. Oklahoma Mesonet stations measure air temperature, humidity, barometric pressure, wind speed and direction, solar radiation, and soil temperatures (McPherson et al. 2007).

The airframe for the SMARTSonde used in this experiment is the Multiplex Funjet Ultra, similar to that used by Reuder et al. (2009). It weighs ≈ 1 kg and has a wingspan of 0.80 m. In the current configuration, the endurance of the airframe with an electric motor is ≈ 30 min with a cruising speed of 15 m s^{-1} . However, this can vary depending on the scientific mission and prevailing wind conditions. The airframe's pusher-prop design allows it to be hand-launched and land on most surfaces. Paparazzi autopilot has been integrated into the platform for autonomous control, although a pilot on the ground is still necessary for take-off and landing (see Bonin et al. 2013a for a more complete description). An inertial measurement unit (IMU) is used to determine the attitude of the airplane and a global positioning system (GPS) receiver provides the position.

An SHT75 sensor by Sensirion is used to take measurements of humidity and temperature. A capacitive sensor is used to measure humidity, while temperature is measured from a band-gap sensor. Based on measurements of the time constant for different airflow conditions and fitting a curve to those measurements, the response time at the typical airspeed of 15 m s^{-1} was found to be 3 s. Accuracies for temperature and relative humidity measurements are 0.3 K and 1.8 %, and the sensor can resolve fluctuations of 0.01 K and 0.05 %. To shield the sensor from direct sunlight, the SHT75 sensor is installed underneath the wing near the body of the fuselage and the sensor is placed inside an opaque tube. Additionally, an SCP1000 sensor by VTI Technologies is installed inside the fuselage to measure atmospheric pressure. The SCP1000 also measures and internally compensates the pressure output for temperature fluctuations. The horizontal wind vector can be extracted from the flight track by using a method outlined in Bonin et al. (2013b).

2.2 Certificate of Authorization

Since the operation of UASs by public institutions in the United States National Airspace System is regulated by the Federal Aviation Administration (FAA), we were first required to obtain a certificate of authorization (COA) to be able to legally fly the SMARTSonde at the KAEFS site. Best practices for FAA COA applications, as outlined by Elston et al. (2011a), were followed. In the process of applying for the COA, a certificate of airworthiness for the SMARTSonde platform was issued by the Department of Aviation at the University of Oklahoma. Moreover, it was necessary to fulfill several safety requirements, including adequate lost link and emergency procedures, loss of GPS signal, runaway aircraft, etc. Four spotters, shown in Fig. 1, were stationed outside the flight path to monitor for other air traffic entering the COA airspace. The pilot-in-command (PIC) maintained constant radio contact with air-traffic control as well as the spotters. The PIC is required to maintain line-of-sight (LOS) contact with the aircraft at all times during flight.

In September 2012, COA 2012-CSA-57 was approved by the FAA for the SMARTSonde to operate within a 1.6-km radius at the KAEFS site up to 914 m a.g.l., with the stipulation that the PIC needs to alert FAA of any flights 48–72 h before operations commence. To fulfill

the COA requirements, the flight pattern used in these experiments was confined to a small circle with a radius of 100 m to keep the aircraft encompassed by the observers, as shown in Fig. 1. The centre of the flight pattern was ≈ 150 m away from the sodar, allowing for a reliable comparison between both measurements. Despite the close proximity of the UAS to the lidar, noise produced by the UAS did not noticeably affect the sodar measurements during the flight times.

3 Calculating the Structure-Function Parameter Using Data from a UAS

While van den Kroonenberg et al. (2012) used a flight path in which the aircraft flew in one direction for several kilometres, making it simple to calculate D_T and C_T^2 based on a moving window along the straight path, the COA granted for the SMARTSonde operations at the KAEFS site does not facilitate such a flight pattern. Instead, a relatively small circular flight pattern as discussed in Sect. 2.2 is used, which limits the maximum distance at which D_T can be calculated. In this flight plan, the UAS platform first circles at the initial height z_1 for a set amount of time. The UAS platform then ascends to the next height z_2 and repeats the circles. This flight pattern is repeated until the highest measurement height is reached. Typically, the UAS platform remains at each height for 3 min, which is the maximum feasible data collection period at each height due to the UAS battery constraints. This flight pattern is referred to as a ‘step-wise ascent’, and the idealized trajectory is shown in Fig. 2.

Values of D_T and C_T^2 are determined for each height at which the UAS collects data over an extended period of time. The separation distance R between each temperature measurement can be calculated by taking the difference between GPS coordinates corresponding to each temperature measurement. These distances and the corresponding temperature differences, ΔT , are separated into bins by range as shown by the coloured lines in Fig. 2. A 20-m bin size was used for this experiment. For each range bin, D_T is calculated using Eq. 1 from

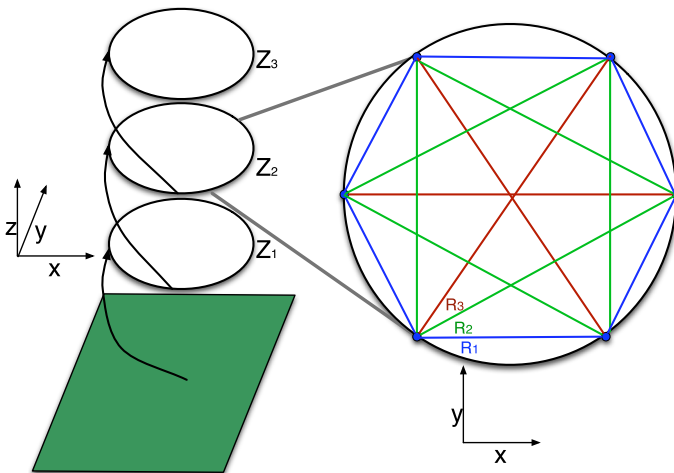


Fig. 2 Idealized trajectory of a SMARTSonde flight for measuring C_T^2 at predetermined heights z_1 , z_2 , and z_3 , where the UAS circles for a predetermined amount of time. The cutout shows how measurements from separation distances R_1 (blue), R_2 (green), and R_3 (red) are binned for averaging. For simplicity, only a few range bins and data points are shown in this diagram. For the flights of interest, the diameter of the circle is 200 m and measurement heights are typically spaced 50 m apart

temperature measurements that are less than 30 s apart, to limit effects on the measurements caused by evolution of the turbulence field. A flight time of 30 s generally corresponds to the completion of half of a circle. Only range bins for which D_T is seen to follow the 2/3 law (Kolmogorov 1941) are used to compute values of mean C_T^2 via Eq. 2, with r the mean R within the range bin.

While the method described above is a fairly straightforward means of calculating D_T and C_T^2 within the UAS sampling domain, it is important to account for the advection of turbulence past the UAS platform, particularly during high wind speeds. To account for this, Taylor's hypothesis of frozen turbulence is utilized (Taylor 1938). Advection can be accounted for in the determination of the separation distance. Instead of calculating R as the simple horizontal distance between two measurement locations, an effective separation distance R_E , which considers the effect of the mean advection of frozen turbulence, can be defined as

$$R_E = \sqrt{(x_2 - x_1 - u \Delta t)^2 + (y_2 - y_1 - v \Delta t)^2}, \quad (5)$$

where x and y are the zonal and meridional separation distances between measurements in m, u and v are the zonal and meridional wind in m s^{-1} , and Δt is the time between measurements in s. R_E is used in place of R to separate the data into bins for calculation of D_T and C_T^2 . With a hygrometer capable of quickly resolving small fluctuations in humidity, this method may also be used to measure C_n^2 from a UAS for comparison with clear-air radar returns.

4 Results and Discussion

For each day of the measurement campaign, the COA was activated for a 2–3 h window of operation 48–72 h before the first planned take-off. Data were collected during the morning hours just after sunrise for half of the days to measure C_T^2 during stably stratified conditions. On the other three days, data were collected in the afternoon during unstable conditions. A large-eddy simulation (LES) was run for the afternoon case presented below, but not for the morning case due to difficulties in reliably simulating turbulence under stable conditions. Specifically, the large-scale forcing data ingested by the LES suffered from an excessive positive temperature bias, while the employed subgrid-scale model overly damped the turbulence. Here, we focus on the observational analysis of data collected at the KAEFS site, and the LES is only used for comparison of profiles of mean quantities. A comparison of various methods for evaluating C_T^2 within the LES, including a virtual UAS employing the measurement strategy discussed in Sect. 3, can be found in Wainwright et al. (2015).

4.1 Environmental Conditions During Case Studies

Data from two cases are presented as the focus of this study. Measurements from the late afternoon of 24 April 2013 will be presented in the first case study and the morning of 28 June 2013 in the second. The presented cases were chosen since data coverage from the UAS and sodar was the greatest within either stability regime, and there were no technical problems with the flights that would affect the data quality. Two UAS flights each with overlapping coverage of the sodar were performed on 24 April, and four flights took place on 28 June. Henceforth, the 24 April case will be referred to as the late afternoon case and the 28 June as the morning transition case.

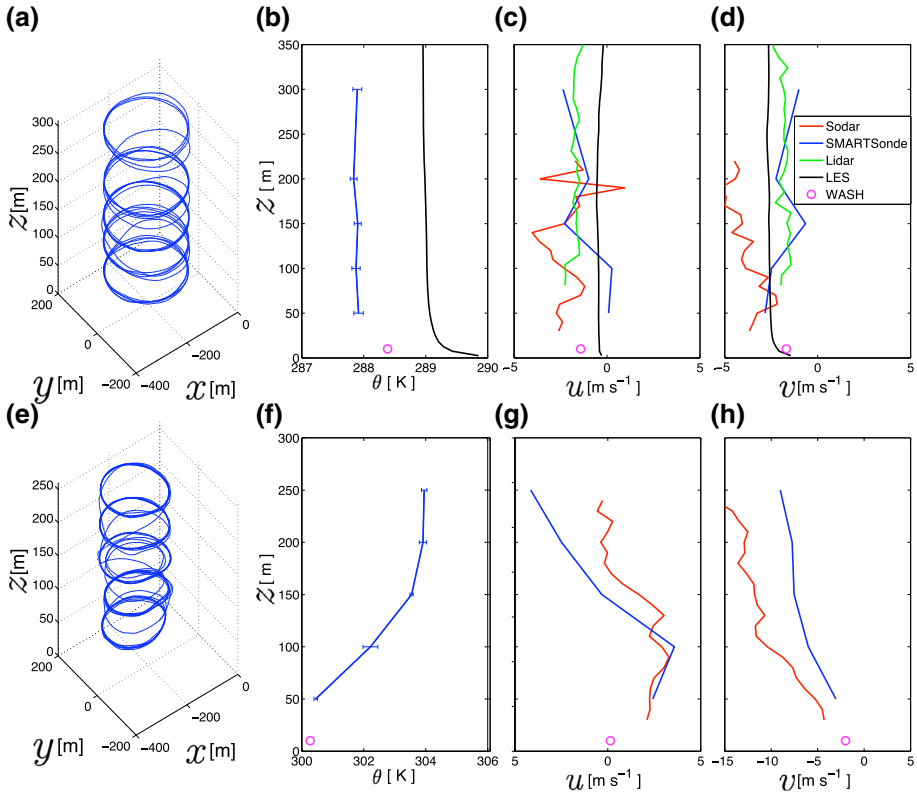


Fig. 3 Flight trajectory and environmental conditions from a selected flight during the **a–d** late afternoon and **e–h** morning transition. Shown are **a, e** real flight trajectories, **b, f** temperature profiles from the SMARTSonde in which *error bars* indicate standard deviation of temperature at each height and a 10-m measurement from the Washington Mesonet site, and **c, g** *u* and **d, h** *v* components of the wind from the sodar (*red*), SMARTSonde (*blue*), lidar (*green*), large-eddy simulation (*black*), and Washington Mesonet site (*magenta circle*)

Flight trajectories, temperature profiles, and wind profiles from the first flight during the late afternoon and second flight during the morning transition are shown in Fig. 3. Flights during the late afternoon took place between 1830–1930 local time (LT, 2330–0030 UTC), and astronomical sunset occurred at 2011 LT. The temperature profile was characteristic of a well-mixed boundary layer, dry adiabatic with a superadiabatic lapse rate near the surface. Based on surface analysis maps, a region of high pressure that was centered over the area resulted in relatively light winds ($\approx 3 \text{ m s}^{-1}$). As the high-pressure area subsequently propagated eastward, the wind direction shifted from northerly to easterly throughout the duration of the flights. The shifting wind direction (see panels c and d of Fig. 3) can partially explain the difference in the SMARTSonde derived winds at various heights, as those measurements were taken over the course of 20 min.

The environment was drastically different from the late afternoon case during the morning transition flights. SMARTSonde measurements were made between 0650–0850 LT (1150–1350 UTC), with astronomical sunrise occurring at 0617 LT. The first flights were made under strongly stable conditions, as evidenced by the potential temperature profile during the second flight in Fig. 3f. During the last two flights, the convective boundary layer began to develop. A cold front had passed over the KAEFS site at 0200 LT, causing the wind direction

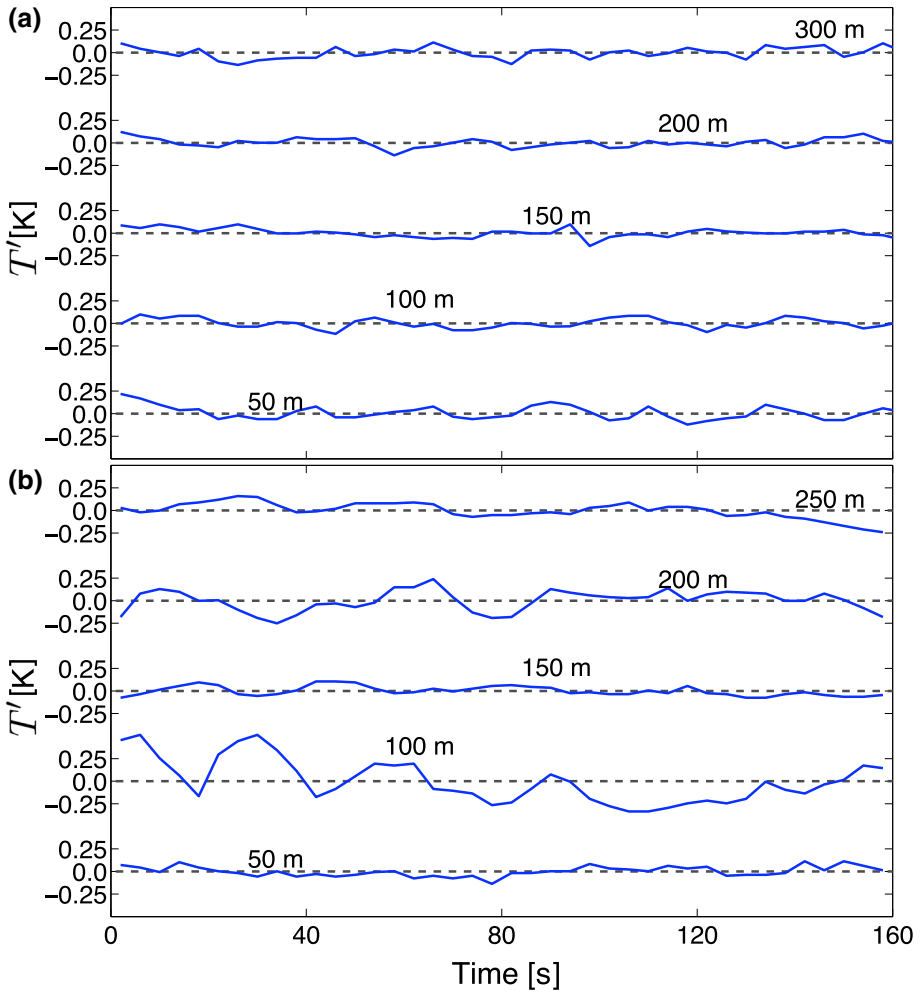


Fig. 4 Time series of observed temperature perturbations from the mean at measurement heights during the **a** late afternoon and **b** morning transition, corresponding to the same flights shown in Fig. 3. Grey dashed lines indicate values of zero fluctuation from the mean at a given height

to shift from southerly to northerly prior to the observational period. During all of the flights, a weak northerly low-level jet was present. While the winds were somewhat variable between each flight, the maximum wind speed was $\approx 10 \text{ m s}^{-1}$ at 100–150 m a.g.l. The wind speed was large enough to affect the performance of the autopilot, with the SMARTSonde oscillating between $\pm 10 \text{ m}$ from the desired flight level as the UAS experienced an increase or decrease in lift depending on the angle of attack. Under typical conditions, these oscillations around the flight level are within $\pm 6 \text{ m}$.

4.2 D_T and C_T^2 Measurements

Temperature traces for each measurement level during one flight, corresponding to the data shown in Fig. 3, from the late afternoon and morning transition are shown in Fig. 4. Generally,

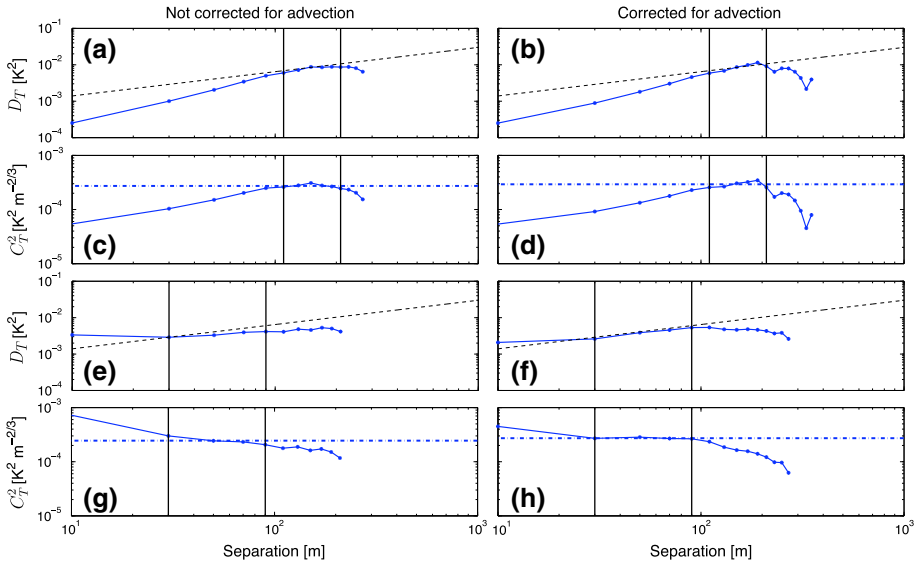


Fig. 5 Temperature structure function with a 2/3 reference line (a, b, e, f) and the structure-function parameter as a function of separation distance between measurements (c, d, g, h). The solid black vertical lines denote the distances in which the inertial subrange is resolved, which is based on where advection corrected D_T follows the 2/3 law. The dashed blue line is the mean value over separations within the resolved inertial subrange. Measurements are from 50 m a.g.l. during the late afternoon (a–d) and morning transition (e–h), corresponding to the same flights shown in Fig. 3. Calculations for data shown in panels on right (b, d, e, g) account for advection of frozen turbulence, while those on the left do not (a, c, d, f)

the temperature variations at each height were below 0.25 K, as would be expected late in the afternoon and during early morning hours since surface heating is weak. However, the temperature fluctuations were still larger than can be explained by the UAS’s variation in height. With a dry adiabatic temperature profile, as observed during the late afternoon, the maximum temperature fluctuation that can be explained by deviations from the desired flight level is 0.1 K, as the UAS typically remained within a ± 6 m range of the desired height. The temperature variance from the morning transition was also greater than can be explained by height oscillations of the SMARTSonde within the measurement layer. The observations at 100 m a.g.l. from the morning transition are the exception, as the UAS struggled due to large wind speeds and oscillated significantly (± 10 m) through the significant inversion layer shown in Fig. 3f. Most of the temperature variance at 100 m a.g.l. on that day can be explained by these oscillations, which is apparent when comparing height and temperature oscillations (not shown). Temperature fluctuations at other flight levels were independent of both height and aircraft heading, which was investigated in order to verify that the sensor was not heated by solar radiation at certain angles causing erroneous measurements.

By calculating ΔT and R from temperature measurements and the corresponding GPS coordinates, D_T and then C_T^2 can be calculated by separating the data into range bins and using the method described in Sect. 3. This yields values of D_T and C_T^2 at each height across a range of separation distances. Values of D_T and C_T^2 at 50 m a.g.l. are shown in Fig. 5 for the first flight from the late afternoon and second flight from the morning transition case. These values correspond to the 50-m temperature traces presented in Fig. 4.

For a non-varying turbulence field, values of C_T^2 are theoretically constant within the inertial subrange when turbulence is locally isotropic and homogeneous (Wyngaard et al.

1971). This range typically extends from a scale of a few millimetres to a few hundred metres (van den Kroonenberg et al. 2012). Herein, the extent of the resolved inertial subrange exists when the D_T values corrected for advection follow the 2/3 law, as within the range bounded by the black lines in Fig. 5b, f. While the inertial subrange theoretically extends down to a few millimetres, the smaller scales of turbulence cannot be resolved, due to the slow response time of the thermistor. Hence, D_T values at small r are seen to not follow the 2/3 law. The mean C_T^2 values for each height and flight, which are compared with the sodar in Sect. 4.3, are calculated by taking the mean value within this resolved inertial subrange.

Correcting for the advection of turbulence is shown to be of particular importance in determining the bounds of the resolved inertial subrange under high wind speeds. For the morning transition case, when a low-level jet was present, D_T only followed the 2/3 law within the inertial subrange after the advection correction had been applied, as seen in Fig. 5e, f. Conversely, the advection correction did not significantly improve the data quality or affect the results from the late afternoon case, where the wind speed was lower. Correcting for advection in the late afternoon data changed the C_T^2 by less than 10 % at every height and flight since the wind speed was low, whereas values of C_T^2 in the morning transition, when wind speeds were higher, changed by more than a factor of 2 for some heights. As such, correcting for the advection of a frozen turbulence field is seen to be important, and this effect may partially explain why UAS-derived C_T^2 values may be overestimated when compared to scintillometer measurements, as discussed by Beyrich et al. (2012), in which an advection correction was not applied. For the remainder of the analysis, the values presented utilize advection correction.

4.3 Comparison with Sodar

As shown in Eq. 4, sodar backscatter is directly related to C_T^2/T^2 , thus sodar returned power can be used to retrieve profiles of C_T^2 . The evolution of the PBL as observed by the sodar before, during, and after the SMARTSonde flights on the two case study days is shown in Fig. 6. Significant changes in the sodar return during each flight period are seen, particularly during the morning transition. This indicates that C_T^2 varies significantly during the time it takes the SMARTSonde to make the observations at the various heights. Since the SMARTSonde also provides vertical profiles of temperature and humidity, the returned power is corrected for atmospheric attenuation before retrieving C_T^2 profiles as detailed in Wainwright et al. (2015). Once C_T^2/T^2 is evaluated from the returned sodar power, C_T^2 can be directly quantified by substituting the temperature measured by the SMARTSonde as T in Eq. 4. As noted earlier, the sodar is uncalibrated. Therefore, an arbitrary scaling factor is applied to the sodar data so that the C_T^2 profiles are of the same magnitude as those from the SMARTSonde. This scaling factor remains constant for all of the comparisons. For each flight, C_T^2 is calculated from the sodar return power from each 5-min interval and the mean returned power over the duration of the flight (25–30 min), which reduces the noise in the profile. This compares with the ≈ 3 min averaging period of the SMARTSonde.

Comparisons of C_T^2 profiles from the sodar and SMARTSonde for different separation distances are shown in Fig. 7. Generally, the SMARTSonde-derived C_T^2 profiles from various R_E are in close agreement within the inertial subrange. At very high and low values of R_E , the computed values of C_T^2 can vary quite drastically due to sensor lag and values outside of the inertial subrange. The shape of the profiles in Fig. 7a roughly agrees with the sodar data, exhibiting a minimum in C_T^2 between 150–200 m with values increasing in height above this level.

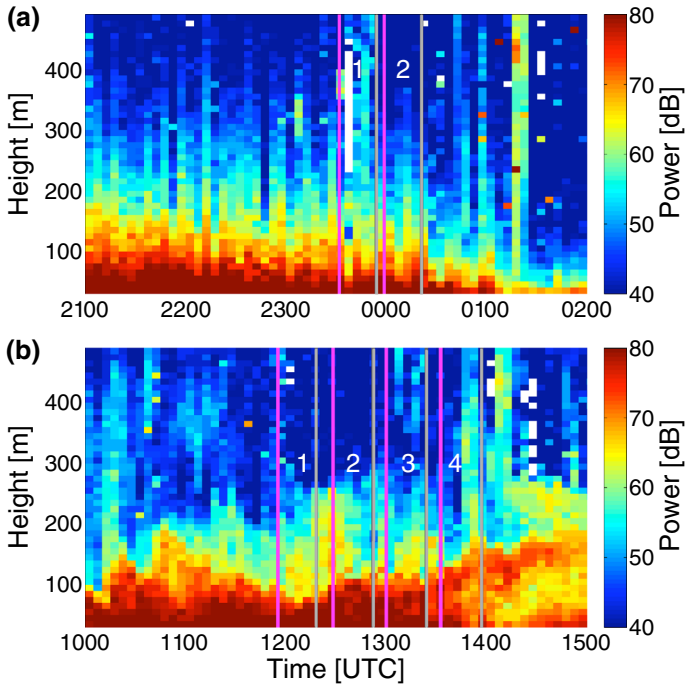


Fig. 6 Sodar return power, not corrected for attenuation or range, during the time flights were conducted during the **a** late afternoon and **b** morning transition. *Magenta lines* mark when each flight started and *grey lines* mark when flights ended. *Numbers* are used as labels for each flight

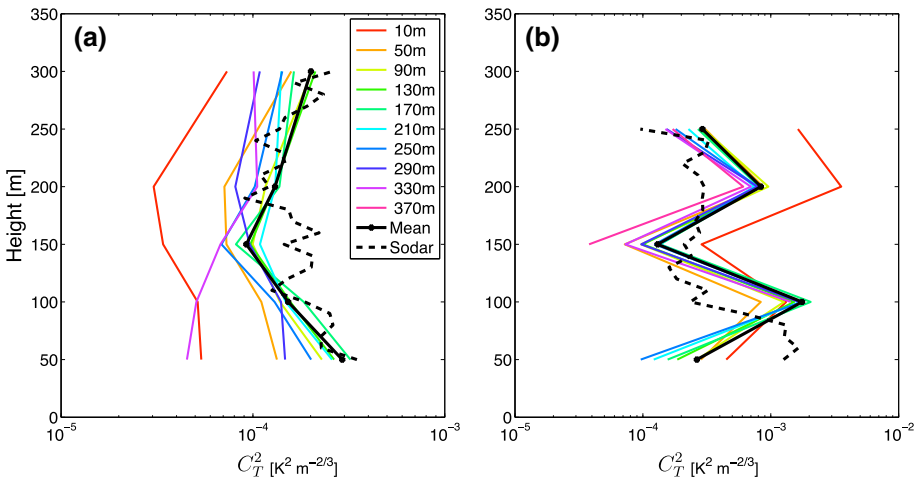


Fig. 7 Comparison of computed C_T^2 at different separation distances with sodar-retrieved values from **a** the first flight from the late afternoon and **b** second flight during the morning transition. This corresponds to the data shown in Fig. 5. *Black solid line* is the mean of C_T^2 at separation distances within the inertial subrange, while the *black dashed line* is the sodar derived values averaged during the time of the flight

In Fig. 7b, the individual profiles of SMARTSonde-derived C_T^2 at differing separation distances again are in good agreement, with the measurements in the 10-m bin being an outlier. The 10-m bin contains the smallest number of total measurement pairs due to high wind speeds causing an increase in R_E . However, there are large differences between the sodar and SMARTSonde C_T^2 profiles. The sodar profile exhibits a sharp decrease in C_T^2 with height between 80–100 m, above which the profile is relatively uniform in height. Conversely, the SMARTSonde C_T^2 profile exhibits two maxima at 100 and 200 m a.g.l. The SMARTSonde-determined C_T^2 at 100 m is erroneously high due to the previously described height oscillations of the UAS platform within this layer due to high wind speeds. Therefore, a considerable portion of the recorded temperature fluctuations cannot be attributed to horizontal inhomogeneities, invalidating some of the assumptions required in the determination of C_T^2 .

The mean C_T^2 , across all separations within the resolved inertial subrange, determined from the SMARTSonde observations for each flight, is compared with the corresponding sodar-derived C_T^2 values in Fig. 8. Once again, the shape of the profiles generally agrees for the late afternoon case, as shown in Fig. 8a, b. As discussed earlier, there is an increase in C_T^2 with height above 150 m from both the UAS and sodar data collected during the first flight. During the second flight, significant differences in the mean C_T^2 profiles between the instruments are present. While both the UAS and sodar generally show lower C_T^2 values than during the first flight, as would be expected later in the evening as turbulence decays, the SMARTSonde measurements do not correspond as closely with the mean C_T^2 profile from the sodar over the duration of the flight. However, each individual SMARTSonde observation between 50–200 m agrees well with the corresponding C_T^2 measurement from the sodar over the shorter 5-min averaging time for both flights during the late afternoon. There are some discrepancies between the 300-m UAS observations, as both are significantly higher than the corresponding sodar estimates. However, the signal-to-noise ratio (SNR) for the sodar is below zero dB at heights above 250 m during the duration of the measurements from the late afternoon. Therefore, the sodar estimates above 250 m are unreliable, especially at 5-min averaging periods.

While the C_T^2 profiles from both instruments agree relatively well during the measurement period in the late afternoon case, significant differences between the C_T^2 profiles from each instrument were noted for the morning transition case as shown in Fig. 8c–f. Additionally, both the SMARTSonde- and sodar-derived profiles exhibited large changes over the 2-h observational window as the convective boundary layer began to develop. For flights one and two during the morning transition case, the sodar SNR dropped below zero dB above 250 m, and above 190 m for flights three and four, indicating that the sodar data are unreliable above those heights. Disregarding the data above those heights, the trends in C_T^2 from both the sodar and SMARTSonde measurements show good general agreement. There is a peak in sodar-derived C_T^2 at ≈ 50 m during the first flight, and the height of that peak rises over the course of the morning. The SMARTSonde also measured a maximum in C_T^2 at similar heights throughout the morning, although the derived C_T^2 values are overestimated at 100 m due to the UAS oscillations through the stable layer.

While the general trends of C_T^2 with height, as derived from both instruments, are in agreement during the morning transition, UAS estimates of C_T^2 tend to be much larger than those from the sodar. In addition to the oscillation of the UAS through a stable layer causing an overestimation in C_T^2 , there was an instance at 250-m height during flight three where the UAS observed two separate prolonged periods (≈ 15 s) where the temperature decreased and then increased by approximately 1 K. While the cause of these large fluctuations in temperature is unknown, the observed fluctuations were likely not a result of isotropic turbulence and thus

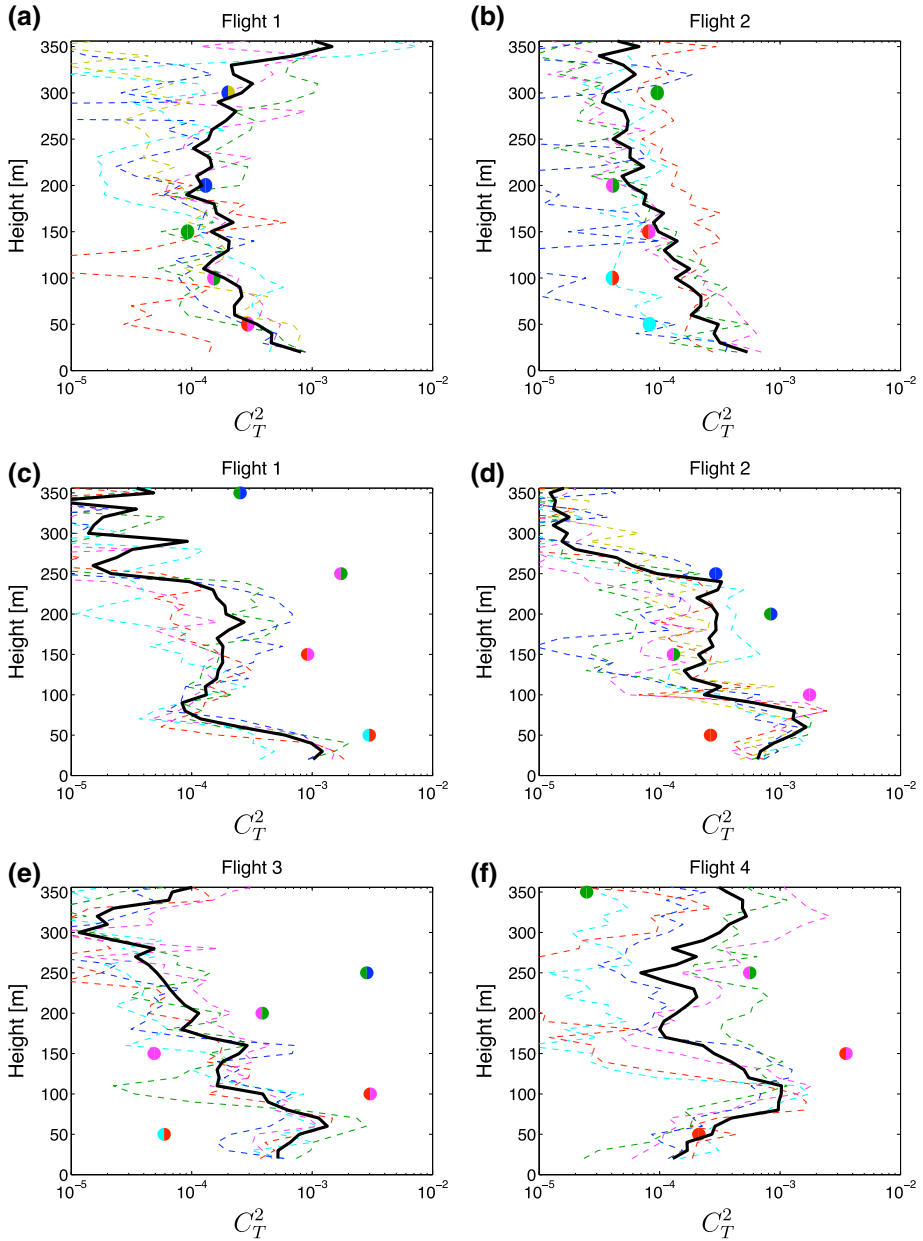


Fig. 8 Comparison of computed mean C_T^2 (units of $K^2 m^{-2/3}$) across separation distances within the inertial subrange from the SMARTSonde (circles) with sodar retrieved values (solid lines) from flights during the **a**, **b** late afternoon and **c–f** morning transition. The time periods for each flight are the same as those delineated in Fig. 6. The thick black line depicts the average C_T^2 profile from the sodar over the duration of each flight (≈ 30 min), while each coloured line shows C_T^2 over each 5-min interval. Each SMARTSonde measurement is colour coded to show the matching sodar observation, with the left (right) colour corresponding to the start (end) time of the SMARTSonde average

should not be used to calculate C_T^2 . While issues such as this are important to consider when using UAS measurements to determine C_T^2 in the stable or transition boundary layer, the agreement in the general shape of the C_T^2 profiles (excluding those measurements impacted by the issues mentioned above) between the instruments demonstrates that the UAS shows promise in measuring C_T^2 in such conditions. In addition, temperature probes with a faster response time would allow for more accurate measurements of C_T^2 . [Wainwright et al. \(2015\)](#) discuss the effect of thermometer response time on the resulting values of C_T^2 .

5 Summary

Two cases are presented in which C_T^2 was determined from temperature measurements made by the SMARTSonde. The two case studies use observations from the stable and unstable boundary layers. The SMARTSonde was flown in a ‘step-wise ascent’ to measure temperature for ≈ 3 min at each height, from which D_T and C_T^2 could be calculated. By assuming that the turbulent eddies move with the mean wind, the observations were corrected for the advection of frozen turbulence by calculating an effective separation distance between measured temperature data points. During the experiment, an Oklahoma Mesonet station and sodar were located at the KAEFS site. A large-eddy simulation was also run for the afternoon case, for which a comparison of measurement methods including a virtual UAS is discussed thoroughly by [Wainwright et al. \(2015\)](#). The sodar return power was used to retrieve C_T^2 profiles for comparison with the SMARTSonde observations.

Overall, the values of C_T^2 were generally constant with separation distance within the resolved inertial subrange, after correcting for the advection of turbulence. While the slow response time of the thermistor did not allow the capture of the inner limit of inertial subrange, the outer limit was always captured. The correction for advection is shown to be important. Without it, being able to delineate where values of D_T followed the 2/3 law was not possible or reliable, especially when the wind speed was high. Additionally, the correction can significantly affect the calculated values of C_T^2 .

Some agreement was noted when comparing C_T^2 profiles derived from the SMARTSonde with those from the sodar. Significant differences in the observed profiles existed during the early morning transition. Many of these differences in the C_T^2 profiles can be explained by:

- Differences in averaging periods. The SMARTSonde averages C_T^2 over 3 min, while the sodar averaging period was ≈ 30 min. Improved agreement was noted when 5-min averages were used from the sodar instead, but the resulting sodar profiles were noisier.
- Rapidly changing environmental conditions from a stable to unstable boundary layer. Profiles of C_T^2 changed significantly between each flight, and even during the flight as the PBL evolved rapidly.
- The UAS sampling within a strong inversion. The UAS oscillated through the inversion, resulting in large fluctuations in temperature that were due to sampling the enhanced vertical temperature gradient. This violated the assumption, for the calculation of C_T^2 , that temperature fluctuations are due to isotropic turbulence. Care needs to be taken in interpreting C_T^2 values from UASs when large temperature gradients are apparent.
- The UAS sampling within the entrainment layer or through gravity waves, where large temperature fluctuations may occur due to PBL phenomena, but are not due to isotropic turbulence.

In the afternoon case study, the C_T^2 profiles showed increased temporal consistency and much better agreement between the instruments. Comparison of these profiles is justified, since many of the necessary assumptions invoked in the determination of C_T^2 from temperature observations were valid, unlike for the morning case. The shape of the profiles agreed well, as did each individual UAS measurement compared to the 5-min data from the sodar.

The method used for this experiment illustrates that UAS can obtain reasonably accurate estimates of C_T^2 in the boundary layer, with the noted caveat that advection must be accounted for. Care needs to be taken when determining C_T^2 with UAS measurements to ensure that recorded temperature fluctuations used to calculate C_T^2 are indeed due to turbulent motions. This is especially true in the stable boundary layer, where turbulence is generally weak and strong temperature gradients often exist. Additionally, UAS-derived C_T^2 values should become more accurate once fast-response thermistors are installed, especially in the stable boundary layer where turbulent scales are much smaller. It may be possible to install two fast response microthermistors in front of both wing tips, which could be used to take temperature measurements used to derive C_T^2 at a certain separation distance. These could be compared with C_T^2 values derived by the method described herein or by that of van den Kroonenberg et al. (2012) to assess the validity of Taylor's frozen turbulence hypothesis.

Acknowledgments The National Science Foundation (NSF) is acknowledged for the support of the reported study through the grant ATM-1016153. We also thank our many colleagues who helped in applying for the certificate of authorization and assisted in the operations of the SMARTSonde at the KAEFS site, especially the Department of Aviation at the University of Oklahoma. We are especially grateful for feedback from the anonymous reviewers, which has improved the quality of this manuscript.

References

- Asanuma J, Iemoto K (2007) Measurements of regional sensible heat flux over Mongolian grassland using large aperture scintillometer. *J Hydrol* 30:58–67
- Beyrich F, Bange J, Hartogensis OK, Raasch S, Braam M, van Dinter D, Gräf D, van Kesteren B, van den Kroonenberg A, Maronga B, Martin S, Moene AF (2012) Towards a validation of scintillometer measurements: the LITFASS-2009 experiment. *Boundary-Layer Meteorol* 144:83–112
- Bonin T, Chilson PB, Zielke B, Fedorovich E (2013a) Observations of early evening boundary layer transitions using a small unmanned aerial system. *Boundary-Layer Meteorol* 146:119–132
- Bonin TA, Chilson PB, Zielke BS, Klein PM, Leeman JR (2013b) Comparison and application of wind retrieval algorithms for small unmanned aerial systems. *Geosci Instrum Method Data Syst* 2:177–187
- Bonner CS, Ashley MCB, Lawrence JS, Luong-Van DM, Storey JWV (2009) SNODAR: an acoustic radar for atmospheric turbulence profiling with 1m resolution. *Acoust Aust* 37:47–51
- Coulter RL, Wesely ML (1980) Estimates of surface heat flux from sodar and laser scintillation measurements in the unstable boundary layer. *J Appl Meteorol* 19:1209–1222
- Danilov SD, Guryanov AE, Kallistratova MA, Petenko IV, Singal SP, Pahwa DR, Gera BS (1994) Simple method of calibration of conventional sodar antenna system. *Int J Remote Sens* 15(2):307–312
- Elston J, Stachura M, Argrow B, Frew E (2011a) Guidelines and best practices for FAA Certificate of Authorization applications for small unmanned aircraft. In: AIAA infotech@aerospace conference, St. Louis
- Elston JS, Roadman J, Stachura M, Argrow B, Houston A, Frew E (2011b) The tempest unmanned aircraft system for in situ observations of tornadic supercells: design and VORTEX2 flight results. *J Field Robot* 28:461–483
- Fairall CW (1991) The humidity and temperature sensitivity of clear-air radars in the convective boundary layer. *J Appl Meteorol* 30:1064–1074
- Gossard E, Chadwick R, Neff W, Moran K (1982) The use of ground-based doppler radars to measure gradients, fluxes, and structure parameters in elevated layers. *J Appl Meteorol* 21:211–226
- Haugen DA, Kaimal JC (1978) Measuring temperature structure parameter profiles with an acoustic sounder. *J Appl Meteorol* 17:895–899

- Holland G, Webster P, Curry J, Tyrell G, Gauntlett D, Brett G, Becker J, Hoag R, Vaglianti W (2001) The aerosonde robotic aircraft: a new paradigm for environmental observations. *Bull Am Meteorol Soc* 82:889–901
- Kanda M, Moriwaki R, Roth M, Oke T (2002) Area-averaged sensible heat flux and a new method to determine zero-plane displacement length over an urban surface using scintillometry. *Boundary-Layer Meteorol* 105:177–193
- Kohsiek W (1982) Measuring c_T^2 , c_q^2 , and c_{TQ} in the unstable surface layer, and relations to the vertical fluxes of heat and moisture. *Boundary-Layer Meteorol* 24:89–107
- Kolmogorov A (1941) The local structure of turbulence in incompressible viscous fluid for very large Reynolds' numbers. *Dokl Akad Nauk SSSR* 30:301–305
- Konrad T, Hill M, Rowland R, Meyer J (1970) A small, radio-controlled aircraft as a platform for meteorological sensors. *Johns Hopkins APL Tech Dig* 10:11–19
- Lagouarde JP, Irvine M, Bonnefond JM, Grimmond CSB, Long N, Oke TR, Salmond JA, Offerle B (2006) Monitoring the sensible heat flux over urban areas using large aperture scintillometry: case study of Marseille city during the Escompte Experiment. *Boundary-Layer Meteorol* 118:449–476
- Mahon R, Moore CI, Burris HR, Rabinovich WS, Stell M, Suite MR, Thomas LM (2009) Analysis of long-term measurements of laser propagation over the Chesapeake Bay. *Appl Optics* 48:2388–2400
- Maronga B, Moene AF, van Dinter D, Raasch S, Bosveld FC, Gioli B (2013) Derivation of structure parameters of temperature and humidity in the convective boundary layer from large-eddy simulations and implications for the interpretation of scintillometer observations. *Boundary-Layer Meteorol* 148:1–30
- Mayer S, Sandvik A, Jonassen M, Reuder J (2010) Atmospheric profiling with the uas sumo: a new perspective for the evaluation of fine-scale atmospheric models. *Meteorol Atmos Phys* 116:1–12
- McPherson RA, Fiebrich CA, Crawford KC, Kilby JR, Grimsley DL, Martinez JE, Basara JB, Illston BG, Morris DA, Kloesel KA, Melvin AD, Shrivastava H, Wolfmberger JM, Bostic JP, Demko DB, Elliott RL, Stadler SJ, Carlson J, Sutherland AJ (2007) Statewide monitoring of the mesoscale environment: a technical update on the Oklahoma Mesonet. *J Atmos Ocean Tech* 24:301–321
- Meijninger WML, Green AE, Hartogensis OK, Kohsiek W, Hoedjes JCB, Zuurbier RM, De Bruin HAR (2002) Determination of area-averaged water vapour fluxes with large aperture and radio wave scintillimeters over a heterogeneous surface - Flevoland field experiment. *Boundary-Layer Meteorol* 105:63–83
- Melnikov VM, Doviak RJ, Zrnić DS, Stensrud DJ (2013) Structures of Bragg scatter observed with the polarimetric WSR-88D. *J Atmos Ocean Tech* 30:1253–1258
- Neff WD (1975) Quantitative evaluation of acoustic echoes from the planetary boundary layer. Technical Report ERL 322-WPL 38, NOAA, Boulder, CO, 34 pp
- Neff WD, Coulter RL (1986) Acoustic remote sensing. In: *Probing the atmospheric boundary layer*. American Meteorological Society, Boston, pp 201–239
- Obukhov A (1949) Structure of the temperature field in a turbulent flow. *Izv Acad Nauk SSSR Ser Geogr Geofiz* 13:58–69
- Petenko I, Argentini S, Pietroni I, Viola A, Mastrantonio G, Casasanta G, Aristidi E, Bouchez G, Agabi A, Bondoux E (2014a) Observations of optically active turbulence in the planetary boundary layer by sodar at the Concordia astronomical observatory, Dome C, Antarctica. *Astron Astrophys* 568:1–10
- Petenko I, Mastrantonio G, Viola A, Pietroni SI (2014b) Some statistics of the temperature structure parameter in the convective boundary layer observed by sodar. *Boundary-Layer Meteorol* 150:215–233
- Puygrenier V, Lohou F, Campistron B, Saïd F, Pigeon G, Bénech B, Serça D (2005) Investigation on the fine structure of sea-breeze during ESCOMPTE experiment. *Atmos Res* 74:329–353
- Reuder J, Brisset P, Jonassen M, Müller M, Mayer S (2009) The Small Unmanned Meteorological Observer SUMO: a new tool for atmospheric boundary layer research. *Meteorol Z* 18:141–147
- Röttger J (1980) Structure and dynamics of the Stratosphere and Mesosphere revealed by VHF radar investigations. *Pure Appl Geophys* 118:494–527
- Shravan Kumar M, Anandan VK, Kesarkar A (2011) Doppler SODAR observations of the temperature structure parameter during monsoon season over a tropical rural station, Gadanki. *J Earth Syst Sci* 120:65–72
- Shuqing M, Hongbin C, Gai W, Yi P, Qiang L (2004) A miniature robotic plane meteorological sounding system. *Adv Atmos Sci* 21:890–896
- Tatarskii VI (1971) The effects of the turbulent atmosphere on wave propagation. *Israel Program for Scientific Translations*, 472 pp
- Taylor GI (1938) The spectrum of turbulence. *Proc Roy Soc A* 164:476–490
- Thomson DW, Coulter RL, Warhaft Z (1978) Simultaneous measurements of turbulence in the lower atmosphere using sodar and aircraft. *J Appl Meteorol* 17:723–734
- van den Kroonenberg A, Martin T, Buschmann M, Bange J, Vorsmann P (2008) Measuring the wind vector using the autonomous mini aerial vehicle M²AV. *J Atmos Ocean Tech* 25:1969–1982

- van den Kroonenberg A, Martin S, Beyrich F, Bange J (2012) Spatially-averaged temperature structure parameter over a heterogeneous surface measured by an unmanned aerial vehicle. *Boundary-Layer Meteorol* 142:55–77
- Wainwright CA, Chilson PB, Gibbs J, Fedorovich E, Bonin T, Palmer R (2015) Methods for evaluation structure functions parameter using unmanned aerial systems and large eddy simulation. *Boundary-Layer Meteorol*. doi:[10.1007/s10546-014-0001-9](https://doi.org/10.1007/s10546-014-0001-9)
- Ward HC, Evans JG, Grimmond CSB (2014) Multi-scale sensible heat fluxes in the suburban environment from large-aperture scintillometry and eddy covariance. *Boundary-Layer Meteorol* 152:65–89
- Weill A, Klapisz C, Strauss B, Baudin F, Jaupart C, Van Grunderbeeck P, Goutorbe JP (1980) Measuring heat flux and structure functions of temperature fluctuations with an acoustic doppler sodar. *J Appl Meteorol* 19:199–205
- Wyngaard J, LeMone M (1980) Behavior of the refractive index structure parameter in the entraining convective boundary layer. *J Atmos Sci* 37:1573–1585
- Wyngaard J, Izumi Y, Collins SA (1971) Behavior of the refractive index structure parameter near the ground. *J Opt Soc Am* 61:1646–1650